Self-Association and Ligand-Induced Conformational Changes of Iron Regulatory Proteins 1 and 2

Emine Yikilmaz,[‡] Tracey A. Rouault,[‡] and Peter Schuck*[,§]

Cell Biology and Metabolism Branch, National Institute of Child Health and Human Development, National Institutes of Health, Bethesda, Maryland, and Protein Biophysics Resource, Division of Bioengineering and Physical Science, ORS, OD, National Institutes of Health, Bethesda, Maryland

Received January 6, 2005; Revised Manuscript Received April 20, 2005

ABSTRACT: Iron regulatory proteins (IRPs) regulate iron metabolism in mammalian cells. We used biophysical techniques to examine the solution properties of apo-IRP1 and apo-IRP2 and the interaction with their RNA ligand, the iron regulatory element (IRE). Sedimentation velocity and equilibrium experiments have shown that apo-IRP1 exists as an equilibrium mixture of monomers and dimers in solution, with an equilibrium dissociation constant in the low micromolar range and slow kinetic exchange between the two forms. However, only monomeric IRP1 is observed in complex with IRE. In contrast, IRP2 exists as monomer in both the apo-IRP2 form and in the IRP2/IRE complex. For both IRPs, sedimentation velocity and dynamic light-scattering experiments show a decrease of the Stokes radius upon binding of IRE. This conformational change was also observed by circular dichroism. Studies with an RNA molecule complementary to IRE indicate that, although specific base interactions can increase the stability of the protein/RNA complex, they are not essential for inducing this conformational change. The dynamic change of the IRP between different oligomeric and conformational states induced by interaction with IRE may play a role in the iron regulatory functions of IRPs.

Cellular iron metabolism is highly regulated because free iron ions can create radicals that can damage the cell. Iron occupies the active sites of many proteins that have major roles in dioxygen transport (hemoglobin, myoglobin, and hemerythrin), scavenging of reactive oxygen species (superoxide dismutase and catalase), nitrogen fixation (nitrogenase), electron transport (cytochromes and ferredoxins), oxygenation and peroxidation reactions (methane monooxygenase, cytochrome P-450, and lipoxygenase), central carbon metabolism (aconitase), and nucleic acid biosynthesis (ribonucleotide reductase). In mammals, intestinal iron uptake is highly regulated and serum transferrin carries iron to tissues and the cells throughout the body (*1*). Mammalian cells regulate the transport and storage of iron through the interaction of the iron regulatory proteins (IRPs) with specific transcripts that encode iron metabolism proteins and iron regulatory elements (IREs) in their 5′ or 3′ untranslated regions (*2*, *3*).

In humans, two different forms of IRPs, which are structural homologues of mitochondrial aconitase, localize to the cytoplasm (*4*). In iron replete cells, IRP1 is a functional aconitase that contains a [4Fe−4S] cluster in its active site, whereas IRP2 lacks aconitase activity. When cells are iron-depleted, both IRPs exert their post-transcriptional gene regulatory effects by binding to IREs (*3*, *5*). Although the two IRPs have high sequence homology to aconitase and both have similar amino acid sequences (Table 1), IRP2 carries a unique 73 amino acid insert that is rich in cysteines, prolines, and glycines. The insert is named iron degradation domain (IDD) because some experimental evidence has previously indicated that IDD is required for ubiquitination and successive proteasomal degradation of IRP2 in response to iron-dependent oxidation (*6*−*8*), although other studies do not support this role (*9*−*11*). It has also been reported that hypoxia stabilizes IRP2 and ubiquitination is a requirement for iron-dependent degradation (*10*, *12*, *13*).

Table 1: Pairwise Sequence Alignments of IRPs and Aconitase

	identity (%)	homology (%)	gaps (%)
IRP1−IRP2	53	70	7
IRP1−aconitase	25	40	16
IRP2−aconitase	24	40	16

The switch of IRP1 from the [4Fe−4S] cluster liganded form with aconitase activity to the IRE-binding activity has been associated with structural changes (*3*, *5*), which have been studied by biochemical methods (*14*−*16*), but only limited biophysical data are available on the size and shape of the proteins in solution (*17*). To gain further insight into the solution structures related to the molecular mechanism of IRPs, we conducted biophysical studies of the oligomeric state and conformational changes by analytical ultracentrifugation, dynamic light scattering, and circular dichroism in the absence of the Fe−S cluster.

EXPERIMENTAL PROCEDURES

Protein Expression and Purification. Details about the construction of the expression plasmids (CA13-02 for IRP1

* To whom correspondence should be addressed: National Institutes of Health, Building 13, Room 3N17, 13 South Drive, Bethesda, MD 20892-5766. Telephone: 301-435-1950. Fax: 301-480-1242. E-mail: pschuck@helix.nih.gov.

[‡] National Institute of Child Health and Human Development, National Institutes of Health.

[§] Division of Bioengineering and Physical Science, ORS, OD, National Institutes of Health.

10.1021/bi0500325
Published on Web 05/19/2005

and CA15-06 for IRP2), protein overexpression in *Pichia pastoris* under the control of strong alcohol oxidase promoter *(AOX1)*, as well as protein purification can be found in ref *18*. Briefly, cultured cells that were grown either by shake-flask or fermentation methods were harvested and kept frozen at −80 °C until needed for purification (*18*, *19*). About 7−10 g of frozen yeast cell pellets are thawed and resuspended in 60 mL of degassed ice-cold lysis buffer. The lysis buffers were composed of 50 mM Tris-HCl, 10 mM KCl, 10 mM NaCl, and 1 mM EDTA at pH 8 that was supplemented with 0.2 mM AEBSF, 3 μg/mL leupeptin, 12.5 μg/mL aprotinin, 0.16 mM deferoxamine mesylate, 8 mM DTT, 4 mM DTPA or EDTA, and complete protease inhibitor cocktail tablets. Either the French press or one-shot cell disrupter (Constant Systems Ltd.) was used at the maximum operational levels of pressure to break the cells. The lysed cells were centrifuged at 31000*g* for 15 min, and the supernatant was applied to size-exclusion chromatography, HiTrap Heparin, HiTrap Q, and IRE-affinity columns as described before (*18*). After the IRE affinity purification column, the protein solution is in high salt (1−1.5 M of NaCl) at pH 8. The proteins were concentrated by ultrafiltration, followed by a final size-exclusion chromatography for buffer exchange. The protein concentration was estimated by using a molar extinction coefficient based on amino acid composition of 84 000 OD_{280}/Mcm for IRP1 and 77 000 OD_{280}/Mcm for IRP2, and IRE concentrations were based on a molar extinction coefficient of 360 000 OD_{260}/Mcm. The protein molar mass from amino acid sequence was 98 390 and 104 995 Da for IRP1 and IRP2, respectively.

Native Gel Protein Shift Assay. Gel-shift assays for the protein samples and the protein/IRE complexes were conducted with a 7.5% native polyacrylamide gel (ProtoGel, National Diagnostics) in TBE buffer. The IRP/IRE complexes migrate faster than the free protein because of high negative charge of the RNA. Purified protein was loaded at micromolar concentrations, which enables staining for the protein (Simply Blue SafeStain, Invitrogen). This assay was described previously in ref *20*. In comparison with routine gel-shift assays in our laboratory with radioactively labeled RNA, smaller gel dimensions and shorter run times are used.

Sedimentation Velocity (SV). SV analytical ultracentrifugation experiments were conducted with an Optima XLI/A (Beckman Coulter, Fullerton, CA). A total of 400 μL samples in 10 mM Tris and 50 mM NaCl at different protein concentrations were used in standard double-sector Epon centerpieces equipped with sapphire windows, inserted in an An60 Ti four-hole rotor. After incubation periods between 4 and 20 h for chemical equilibrium of the diluted protein sample to be attained, interference data were acquired at rotor speeds of 40 000−60 000 rpm and at a temperature of 20 °C. The solvent density of 1.0006 g/mL and viscosity of 1.009 cPoise was calculated using the software SEDNTERP, kindly provided by Dr. J. Philo. For studies of the interaction of IRP proteins with IRE, absorbance data at a wavelength of 260 nm were acquired simultaneously to the interference data. Data were analyzed using the $c(s)$ continuous distribution of Lamm equation solutions (*21*) with the software SEDFIT. In brief, the experimental sedimentation profiles $a(r,t)$ were modeled as superpositions

$$a(r,t) \cong \int_{s_{min}}^{s_{max}} c(s)\chi(s,D(s),r,t)\mathrm{d}s + a_{TI}(r) + a_{RI}(t) \quad (1)$$

of solutions of the Lamm equation

$$\frac{\partial \chi}{\partial t} = \frac{1}{r}\frac{\partial}{\partial r}\left[rD\frac{\partial \chi}{\partial r} - s\omega^2 r^2 \chi\right] \quad (2)$$

(with r denoting the distance from the center of rotation, ω being the angular velocity, and s and D being the sedimentation and diffusion coefficients, respectively) (*22*), calculated by finite element methods (*23*). The diffusion coefficients D were estimated through a weight-average frictional ratio f/f_0 as

$$D(s) = \frac{\sqrt{2}}{18\pi} kTs^{-1/2}(\eta(f/f_0)_w)^{-3/2}((1-\bar{v}\rho)/\bar{v})^{1/2} \quad (3)$$

(with ρ and η denoting the solution density and viscosity, respectively, $\bar{v}$ being the protein partial-specific volume, T being the absolute temperature, and k being the Boltzmann constant) (*24*). The time-invariant signal contributions $a_{TI}(r)$ and the radial-invariant offsets $a_{RI}(t)$ were calculated by algebraic noise decomposition (*25*). The integral equation was solved with maximum entropy regularization. A detailed description of this approach can be found in ref *24*. The weight-average frictional ratio and the meniscus position of the sample were optimized by nonlinear regression, leading to final rms errors of the sedimentation model of <0.01 fringes. For analysis of the slow reacting monomer−dimer system, peaks of the $c(s)$ distributions were integrated and the isotherm of species populations as a function of loading concentrations was globally modeled using the software SEDPHAT.

For studying the monomer−dimer self-association kinetics, the SV data were modeled with finite element solution of sets of Lamm equations coupled by fluxes j representing the chemical reaction kinetics

$$\frac{\partial \chi_i}{\partial t} - \frac{1}{r}\frac{\partial}{\partial r}\left[rD\frac{\partial \chi_i}{\partial r} - s\omega^2 r^2 \chi_i\right] = j_i \quad \text{for } i = 1, 2$$

$$j_1 = -2j_2 = k_{off,2}(2\chi_2 - K_{12}\chi_1^2) \quad (4)$$

with χ_1 and χ_2 denoting the local molar concentrations of monomer and dimer, respectively, K_{12} denoting the equilibrium association constant, and $k_{off,2}$ denoting the chemical off-rate constant for dimer dissociation (*26*). Best-fit time-invariant and radial-invariant noise components were superimposed to the theoretical profiles. Modeling was performed with the software SEDPHAT (*27*).

Sedimentation Equilibrium. Sedimentation equilibrium experiments were conducted at 4 °C in an Optima XLI/A (Beckman Coulter, Fullerton, CA) at rotor speeds of 8000, 12 000, and 15 000 rpm in double-sector Epon centerpieces. Absorbance data at wavelengths of 280, 250, and 230 nm were acquired from samples at three loading concentrations at all rotor speeds. The protein partial-specific volumes (0.740 and 0.741 mL/g for IRP1 and IRP2, respectively) and the extinction coefficients at 280 nm (see above) were predicted from the amino acid composition using the software SEDNTERP. Global nonlinear regression of the experimental absorbance profiles $a_\lambda(r)$ was performed using SEDPHAT

(*27*), using the equations for the radial concentration distribution of a monomer−dimer system in reversible self-association and sedimentation equilibrium

$$a_\lambda(r) = c_1(r_0)\epsilon_\lambda d \exp\left[M(1-\bar{v}\rho)\frac{\omega^2(r^2-r_0{}^2)}{2RT}\right] + 2K_{12}c_1(r_0)^2\epsilon_\lambda d \exp\left[2M(1-\bar{v}\rho)\frac{\omega^2(r^2-r_0{}^2)}{2RT}\right] \quad (5)$$

where $c_1(r_0)$ denotes the monomer concentration at the reference radius r_0, ϵ_λ is the molar extinction coefficient, d is the optical path length, R is the gas constant, and M is the protein molar mass. This was combined with time-invariant noise elimination, consideration of incompetent monomer fractions, and/or mass conservation constraints (*28*). Error estimates were obtained by projections of the error surface and F statistics.

Dynamic Light Scattering. Autocorrelation functions were acquired using a Protein Solutions DynaPro 99 instrument with a DynaPro-MSTC200 microsampler (Protein Solutions, Charlottesville, VA). The scattering signal was observed at an angle of 90°, a wavelength of 808.3 nm, and a temperature of 20 °C. Data acquisition and initial analysis were performed with the instrument software, and data were exported for analysis with the maximum entropy method and with discrete species models in the software SEDFIT.

Circular Dichroism (CD). CD spectra were measured in a Jasco J-810 spectropolarimeter (Jasco Inc., Easton, MD). For each measurement, three spectra were acquired at a rate of 100 nm/min with a time constant of 2 s. Spectra of IRP and IRE at about 1−2 μM in 10 mM potassium phosphate at pH 8.1 and mixtures of 1:1 molar ratio were measured at a temperature of 20 °C, using rectangular quartz cuvettes of 1 or 2 mm path length, respectively. Secondary structure was estimated with the software CDPro, and values returned from SELCON3 (*29*), CONTINLL (*30*), and CDSSTR (*31*) were averaged. For comparison, the secondary structure was predicted using PHD (Rost and Sander, 1994).

RESULTS

First, we studied the oligomeric state of IRP1 in solution. SV profiles of IRP1 exhibit clearly bimodal sedimentation boundaries, demonstrating the presence of two oligomeric states of the protein (Figure 1). The $c(s)$ analysis of sedimentation coefficient distributions shows peaks with concentration-independent peak positions but with peak areas dependent on the loading concentration, indicating the presence of a slow equilibrium. After the initial observation of the slow monomer−dimer dissociation, the SV experiments were repeated with long incubation periods of the sample after dilution for a self-association equilibrium to be attained prior to the start of the run. The SV data can be fit well with a direct boundary model for monomer−dimer self-association, with a best-fit equilibrium constant of $K_D \sim 1-2$ μM, a rate constant of $k_{off} \sim (5-8) \times 10^{-5}$ s^{-1}, and sedimentation coefficients for the monomer and dimer of 5.4 and 8.4 S, respectively. Similar results were obtained from experiments with different preparations of the protein conducted at rotor speeds between 40 000 and 60 000 rpm. The sedimentation coefficients for the monomer and dimer correspond to hydrodynamic frictional ratios of 1.35 and 1.39, respectively, both indicating essentially globular, slightly asymmetric solution structures. Because the reaction is slow compared to the time scale of the SV experiments (the estimated lifetime of the complex is approximately twice the sedimentation time at 60 000 rpm), the sedimentation coefficient distributions $c(s)$ can be calculated as a function of the loading concentration and the peak areas represent the populations of the monomeric and dimeric species. As shown in Figure 1, with an increasing loading concentration, the fraction of dimer increases, as expected for a reversible equilibrium. As a second test for reversibility, we conducted two sequential SV experiments of the same sample, first to

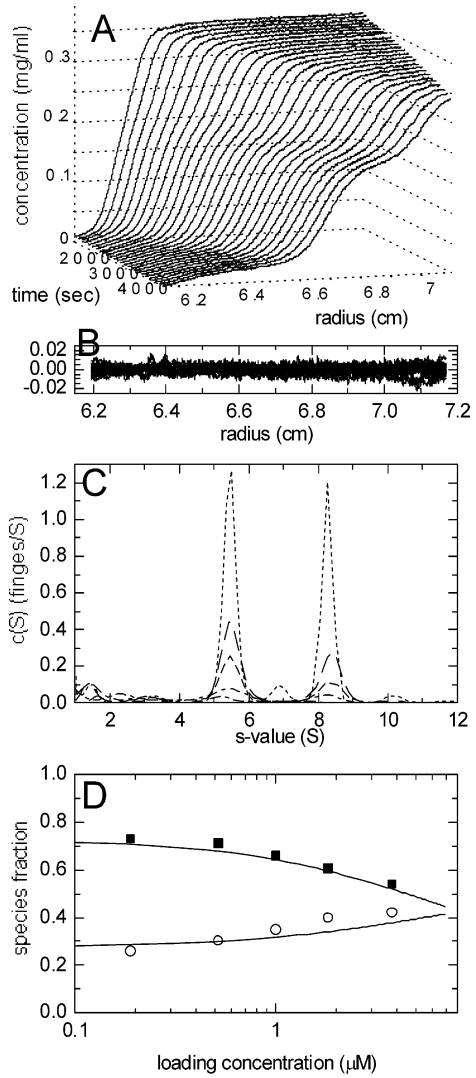

FIGURE 1: SV experiments of IRP1 reveal the presence of monomers and dimers in a slow reversible equilibrium. (A) Evolution of the concentration profiles of 4.5 μM IRP1 in 10 mM Tris and 50 mM NaCl at pH 8.0 at a rotor speed of 60 000 rpm (data shown are in 2 min intervals). Analysis of the data with a model for reversibly reacting monomer−dimer self-association yields an estimated equilibrium constant of $K_D \sim 1$ μM and a reaction rate constant of $k_{off} \sim 5 \times 10^{-5}$ s^{-1} (also taking into account a trace contamination of 2% of a high molar mass species at 11.3 S). (B) Residuals of the fit in units of fringes. (C) Sedimentation coefficient distributions $c(s)$ at loading concentrations of 4.5 (···), 2.25 (− − −), 1.35 (- - -), 0.45 (-·-), and 0.23 μM (—) IRP1. (D) Relative populations of monomeric (■) and dimeric (○) species as a function of total loading concentration, calculated by integration of the $c(s)$ distributions. Solid lines are the best-fit isotherms with estimates of $K_D \sim 10$ μM in the presence of a fraction of 0.28 incompetent dimer.

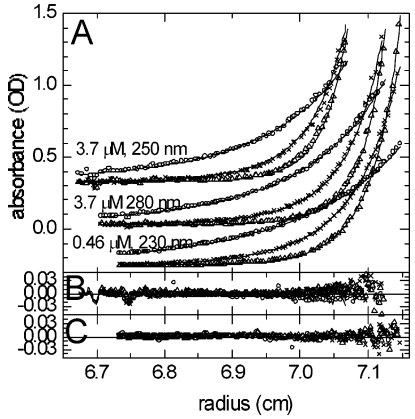

FIGURE 2: Sedimentation equilibrium analysis of the monomer−dimer self-association equilibrium of IRP1. (A) Sedimentation equilibrium absorbance profiles of IRP1 at rotor speeds of 8000 rpm (○), 12 000 rpm (×), and 15 000 rpm (△). Loading concentrations were 3.71, 1.23, and 0.46 μM, and absorbance scans were acquired at wavelengths of 280, 250, and 230 nm. Data shown are at the loading concentration of 3.71 μM at 250 nm (scaled by factor 2 and offset by 0.3 OD vertically and 0.05 cm horizontally), 3.71 μM at 280 nm (original scale), and 0.46 μM scanned at 230 nm (offset by −0.3 OD vertically). For clarity, only every second data point is shown. Solid lines are the best-fit distributions from global analysis including soft mass balance constraints (*28*). The best-fit dimerization constant is $K_D = 7.7$ μM (with an error interval from 6.9 to 8.9 μM). (B) Residuals of the fit for the 3.71 μM data, with symbols for the residuals to the 280 nm scans and lines for the 250 nm scans. (C) Residuals of the fit for the 0.46 μM data. The overall rms deviation of the fit is 0.0087 OD.

establish the initial population of monomer and dimer, followed by a 15 h concentration period in the centrifugal cell at 60 000 rpm, and finally a second SV run after resuspending the protein without re-equilibration of the self-association equilibrium. As expected, a higher fraction of dimer was observed after concentration, but unfortunately, no complete resuspension of the protein was achieved (data not shown).

The analysis of the isotherm of species populations suggest an equilibrium dissociation constant of ∼10 μM. The slightly higher estimate of the K_D and the significant fraction of apparently nondissociated dimer may indicate imperfect chemical equilibrium after dilution of the stock concentration prior to the start of the SV experiments, despite the extended incubation period. This highlights the difficulties of this approach and raises the possibility that the off-rate constant estimated from modeling the shape of the sedimentation boundaries may be an overestimate and/or that the dimer may exist in different conformations with different dissociation rate constants (see below).

To examine the monomer−dimer self-association more closely and to obtain an estimate for the dimerization constant independent of the complications due to the reaction kinetics, sedimentation equilibrium experiments were performed with IRP1 (Figure 2). The global analysis of absorbance profiles acquired over a wide range of concentrations and rotor speeds resulted in an excellent fit, with $K_D = 7.7$ (6.9−8.9) μM. (A similar result with a K_D value of 11 μM was achieved if incompetent dimer was considered, with a best-fit estimate of 11%.) Together with the estimate for the lifetime of the dimer from SV, we can estimate the on-rate constant for dimer formation to be in the order of $k_{on,12} \sim 10\ M^{-1}\ s^{-1}$.

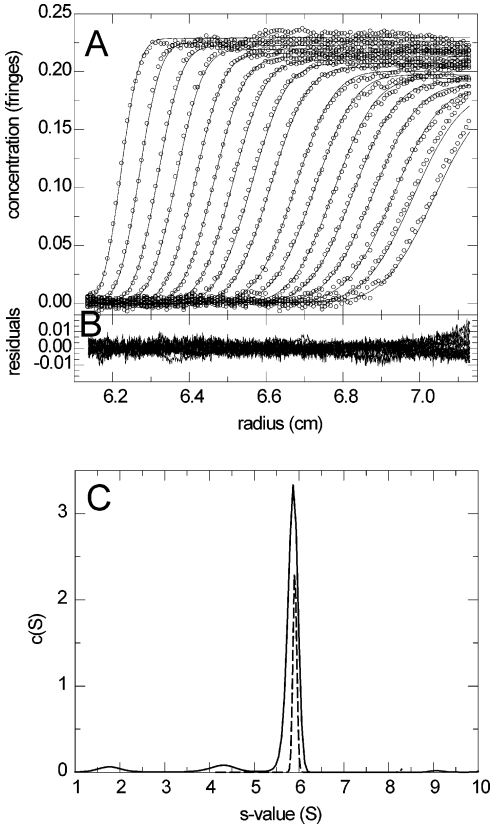

FIGURE 3: Oligomeric state of IRP2 by SV reveals a monomeric protein. (A) SV interference profiles of 0.7 μM IRP2 at a rotor speed of 50 000 rpm (○, for clarity, only every 4th scan and every 10th radial point is shown) and a single-species Lamm equation fit (solid line), which leads to a value of $s_{20,w}$ of 5.88 S and an apparent molar mass of 111.8 (±1.5) kDa. (B) Residuals of the fit with a rms deviation of 0.0027 fringes. (C) Sedimentation coefficient distributions $c(s)$ at 0.7 μM (- - -) and 3 μM (—).

Next, we studied the solution association state of IRP2. Representative SV profiles of IRP2 are shown in Figure 3. In contrast to those of IRP1, they are not bimodal but can be described well with a single species Lamm equation solution with a molar mass of 112 kDa and a sedimentation coefficient of $s_{20,w}$ of 5.88 S. Considering the common uncertainty of the protein partial specific volume, this molar mass is consistent with that of the monomer (sequence molar mass of 105 kDa). We found no evidence of dimer formation in the sedimentation coefficient distributions (Figure 3C) and no indications of a concentration dependence characteristic for self-association. The measurement of the translational diffusion coefficient by dynamic light scattering gave a value of $D = 4.6 \times 10^{-7}$ cm^2/s that corresponds, in combination with the sedimentation coefficient, to a molar mass of 122 kDa, reasonably consistent with the monomer molar mass. The hydrodynamic data lead to a frictional ratio of 1.30, indicating a slightly more compact solution structure than IRP1.

The study of the interaction of IRPs with IRE was conducted with 36-mer oligomer RNAs derived from modified H-ferritin IRE (Figure 4A), IRE-C. It is similar to wild-type ferritin H-chain IRE for which the NMR structure has been reported (*32*, *33*). To ascertain to what extent the binding properties are due to base-specific interactions, a second oligomer was constructed with the complementary sequence, IRE-N (Figure 4B). Because the designed sequence

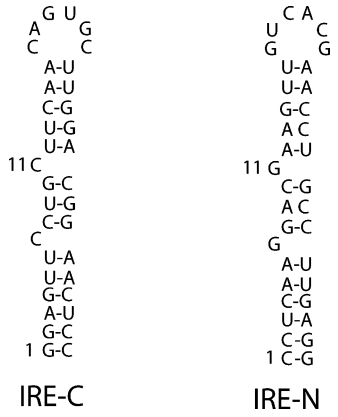

FIGURE 4: Schematic representations of secondary structure elements in 36-mer oligonucletide RNAs. (A) Modified H-ferritin IRE fragment. (B) IRE-N has a complementary sequence to H-ferritin RNA.

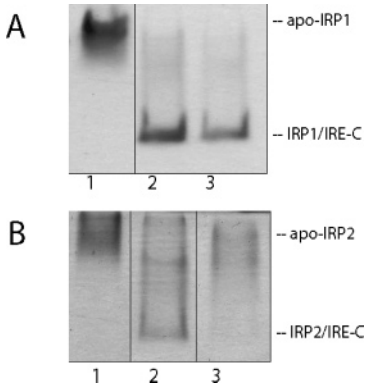

FIGURE 5: Native gel assays for IRP samples indicate efficient RNA−protein complex formation. (A) 3.8 μM IRP1 (lane 1) and 2 and 1 μM equimolar IRP1/IRE-C complexes (lanes 2 and 3). (B) 1 μM IRP2 (lane 1), 0.7 μM equimolar IRP2/IRE-C complex (lane 2), and 0.7 μM equimolar IRP2/IRE-N complex (lane 3). The IRP/IRE complexes move faster compared to the IRPs because of the high negative charge of IREs.

for IRE-N is complementary to the IRE-C sequence, the final shapes of the two RNAs may be assumed to exhibit similar hairpin conformations and base-stacking interactions.

It has been established that the IRP−IRE binding affinity is in the picomolar range, of 1:1 stoichiometry, and with slow dissociation (*34*, *35*). Gel competition experiments and surface plasmon resonance experiments in our laboratory gave results consistent with this high-affinity interaction (unpublished data). For the present study, the binding of IRE to the recombinant IRP was first characterized qualitatively by native PAGE electrophoresis followed by staining the protein (Figure 5). This assay allows us to compare the stability of the complex, and because of the high loading concentration permitting protein staining, the assessment if the protein is homogeneously active. The IRP/IRE complexes migrate faster than the apoprotein because of a high negative charge of the nucleic acid (*20*). For IRP1, tight complexes with lifetimes greater than the time scale of the electrophoresis experiments were formed with IRE-C (Figure 5A). IRP2 formed a relatively stable complex with IRE-C, but IRE-N partially dissociated during the electrophoresis (Figure 5B). These experiments demonstrate that the IRP samples exhibit a high degree of IRE-binding activity and suggest that specific base interactions (presumed absent in IRE-N)

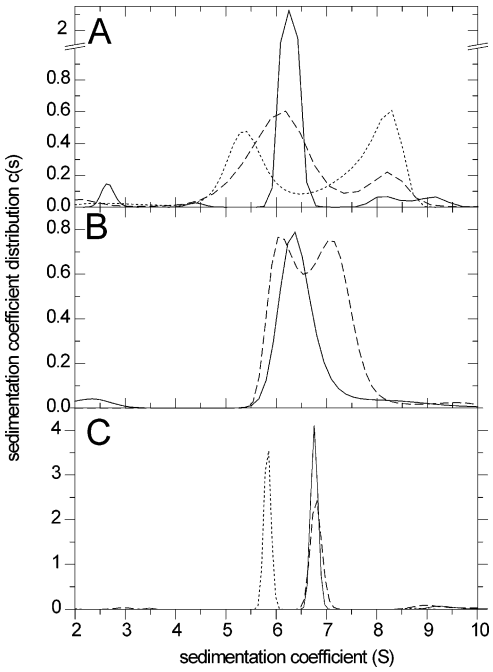

FIGURE 6: Interactions of IRP1 and IRP2 with IRE studied by SV. (A) Sedimentation coefficient distributions $c(s)$ of 4.4 μM IRP1 alone (···) and in mixture with 1.5 μM IRE-C (- - -) and 4.5 μM IRE-C (—). The SV data were acquired with interference optical detection. (B) Sedimentation coefficient distributions $c(s)$ from a dual-detection SV experiment with a mixture of 5 μM IRP1 and 2 μM IRE-C observed with absorbance optics at 260 nm (—) and with interference optics (- - -). (C) $c(s)$ distributions of IRP2 (2.2 μM) in the absence (···) and presence (—) of equimolar IRE-C, derived from the interference optical system. For comparison, the equimolar mixture with the complementary IRE-N is shown (- - -).

do contribute to the stability of the complex by decreasing the dissociation rate constant and/or increasing the binding energy.

The mode of interaction of the IRPs with IRE in solution was studied in more detail by analytical ultracentrifugation. SV experiments of mixtures at different molar ratios of IRP1 and IRE-C were performed. The signal from 4.4 μM IRP1 is shown in Figure 6A as a dotted line. After addition of increasing concentrations of IRE-C to a constant amount of IRP1, a concentration-dependent shift in the $c(s)$ profiles is observed toward a single peak. With IRE-C in a slight molar excess, nearly all of the IRP1 is converted into a ~6.2 S peak. Although this s value could theoretically reflect a highly extended dimer, this can be ruled out based on sedimentation equilibrium experiments, which resulted in a weight-average molar mass of 102 kDa (data not shown). For the IRP1/IRE-C complex with 1:1 stoichiometry, one could expect a slightly higher s value than the IRP1 monomer alone, because of the added mass of the nucleic acid (a back-of-the-envelope estimate assuming the same hydrodynamic shape as the IRP1 monomer would suggest an s value of a complex with the added mass of 11.5 kDa of ~5.8 S, and an estimate assuming the nucleic acid to be completely buried inside the protein would give an s value of 6.0 S). However, the observed increase to 6.2 S is much larger than expected, which suggests that the protein changes to a hydrodynamically more compact structure upon complex formation (a conformational change was confirmed by CD, see below). The shift from the monomer−dimer self-association toward

a single complex with IRP1 monomer demonstrates that IRE-C preferentially interacts with the IRP1 monomer.

The preference of IRE-C for binding to the IRP1 was confirmed by a dual-detection SV experiment using refractive index and absorbance signals at 260 nm. For the protein, the refractive index signal is much larger than the absorbance signal and, conversely, for the IRE-C, the absorbance signal is much larger than the refractive index signal, thus approaching selective detection. Figure 6B shows the resulting sedimentation coefficient distributions from a mixture with an intermediate ratio of IRP1 to IRE-C (5 μM IRP1 and 2 μM IRE-C), where bound and unbound species should coexist. Strikingly, the absorbance traces (—) show only a single peak for the IRP1 monomer/IRE-C complex, whereas the refractive index signal from the same experiment (- - -) shows the coexistence of unbound monomer and dimer (although not hydrodynamically resolved). This illustrates that the IRE-C binds preferentially to the IRP1 monomer. Further, the fact that the *s* value of the IRP1/IRE-C complex for substoichiometric loading concentrations of IRE-C (Figure 6B, —) is identical to the *s* value of the complex when IRE-C is in excess (Figure 6A, —) is consistent with the formation of a very stable, high-affinity and saturable interaction (*26*), as can be expected from the literature.

Analogously, we conducted SV studies on the IRE interaction with IRP2. Similar to IRP1, the IRP2/IRE-C complex also exhibits a significantly higher sedimentation coefficient than the uncomplexed IRP2 monomer (Figure 6C). This was observed for IRE-C and IRE-N. In the hydrodynamic studies with IRP2, both the free protein and the complex were well-described by a model for a single sedimenting species. Therefore, these samples lend themselves well to dynamic light scattering. In these experiments, we measured an increase of the diffusion coefficient by 10% for the equimolar mixture of IRE-C and IRP2 as compared to IRP2 alone. This corresponds to a 10% decrease in the Stokes radius of the IRP2/IRE-C complex as compared to free IRP2. This unequivocally demonstrates that the increase in the sedimentation coefficient is due to a more hydrodynamically compact shape of the complex. The ability to model the sedimentation boundaries from equimolar IRP2 and nucleic acid as single species with negligible free protein or free nucleic acid also demonstrates the high-affinity interaction of IRP2 with both IRE-C and IRE-N, with K_D values for both far below the concentration used in the present experiments. Because the kinetics of the interaction of IRP2 with IRE-N seems to be faster as compared to IRE-N (see above), the coincidence of the peak positions of $c(s)$ in Figure 6C further supports that complex formation is of high-affinity and saturated for both RNA molecules under the experimental conditions (*26*).

The protein secondary structure and the conformational changes in the presence of IRE were studied further by CD spectroscopy. The CD spectra of IRP1 and IRP2 are shown in parts A and B of Figure 7, respectively (—). From the quantitative modeling of the experimental CD spectra, we estimated ~25% helix and ~25% sheet content for both IRP1 and IRP2. Within the uncertainty of this determination, the measured secondary structural elements appear consistent with those theoretically predicted from the sequence homology with aconitase (Tables 1 and 2), The CD signals of IRE-C and IRE-N (Figures 8A) were consistent with those

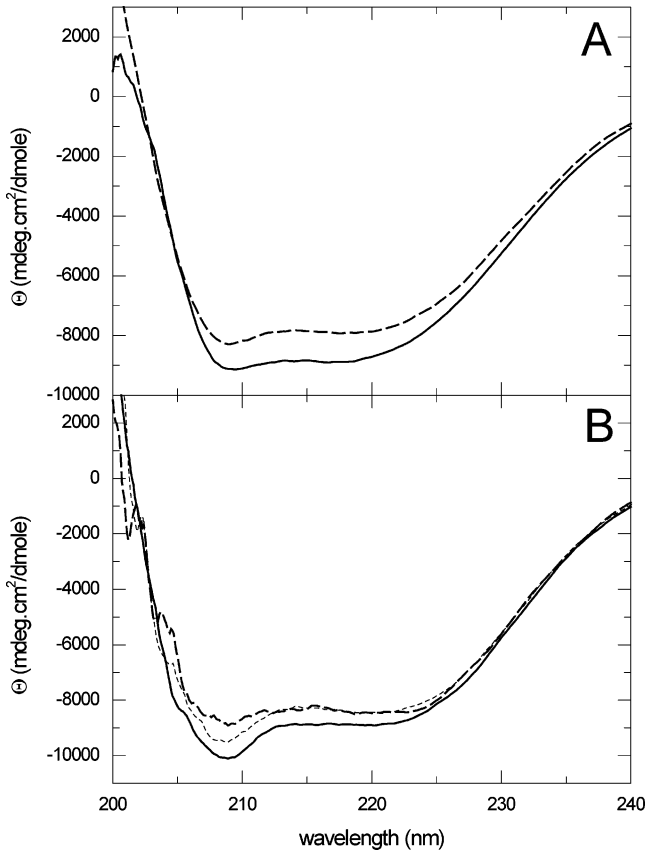

FIGURE 7: CD spectra of IRP in the absence and presence of equimolar IRE-C. (A) apo-IRP1 (—) and the measured complex IRP1—IRE-C minus the theoretical contribution of IRE-C in the mixture (- - -). (B) apo-IRP2 (—) and the measured complex IRP1—IRE-C minus the theoretical contribution of IRE-C in the mixture (- - -). The analogous CD spectrum of IRP2 in complex with an oligonucleotide comprising the stem loop of IRE-C only is also shown (•••). For both the proteins, CD is expressed as molar ellipticity per residue.

expected for double-stranded A-form DNAs or RNA (*36*, *37*) and were similar for both forms.

The CD spectra of the mixtures clearly deviate from those of the individual components, indicating changes in secondary structure upon complex formation. This was observed for protein—IRE mixtures using IRP1 (Figure 7A) or IRP2 (Figure 7B), as well as for IRE-C and IRE-N (Figure 8B). The CD features of the change in secondary structure are a decrease in the ellipticity in the range from 205 —230 nm and an increase at 200 nm. An oligonucleotide resembling IRE-C but missing the hairpin loop CAGUGC also induced a conformational change (•••, Figure 7B) of similar magnitude but with less change at 208 nm. The spectra of the nucleic acids IRE-C and IRE-N are similar (Figure 8A). No change in the spectrum in the wavelength range greater than 250 nm was detected when IRE-C or IRE-N were in the mixture with IRP2 (Figure 8B). Usually, this spectral range reports on changes in the nucleic acid secondary structure (*38*). The absence of changes above 250 nm suggests that the observed CD signature of the conformational changes of complex formation reflect changes in the structural elements in the protein conformation (*38*), consistent with the altered hydrodynamic friction (see above). With this assumption, the altered CD spectra correspond for IRP1 to an increase in the total helix content by 2% and no change

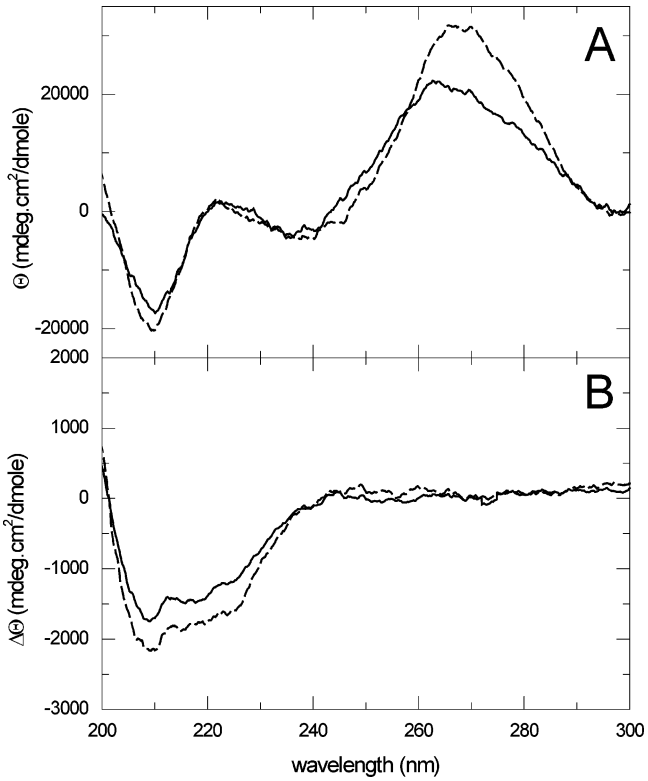

FIGURE 8: CD spectra of the nucleic acids IRE-C and IRE-N and the conformational changes induced after binding of IRP2. (A) Molar ellipticity per base of IRE-C (—) and the complementary IRE-N (- - -). (B) Difference spectra of IRP2 in the presence and absence of IRE (apo-IRP2 spectra minus IRP2−IRE complexes corrected for the IRE contribution) for IRE-C (—) and the complementary IRE-N (- - -). CD is expressed as molar ellipticity per protein residue.

Table 2: Secondary-Structure Elements as Predicted, Calculated from CD Spectra, and Calculated from the Structural Model of 8ACN

protein	helix	sheet	loop
IRP1 (predicted)	32	17	51
IRP1 (experimental)	25	24	
IRP2 (predicted)	30	17	53
IRP2 (experimental)	25	25	
aconitase (structure)	32	18	50

in the total sheet content and for IRP2 a loss of helix content by 5% and an increase in sheet content by 2%.

DISCUSSION

In the present study, we have used biophysical techniques to characterize the solution structures of IRP1 and IRP2 free and in complex with IRE. We found that apo-IRP1 exists in a slowly reversible monomer−dimer self-association equilibrium and that binding of IRE drives a conformational change toward a more compact complex in which IRP1 is entirely monomeric. In contrast, IRP2 did not show detectable dimerization but also became more compact in the presence of IRE.

In regard to the size and shape of the IRPs, the measured translational friction coefficient indicates that the protein is moderately compact. The hydrodynamic Stokes radius of the monomer and dimer was 4.2 and 5.4 nm, respectively. Brazzolotto and colleagues have determined a radius of gyration of 4.0 nm for apo-IRP1 by neutron scattering (*17*). Differences between the radii of gyration and the Stokes radii can be expected because the latter is determined essentially by the surface of the protein, whereas the radius of gyration is dependent on the mass distribution. For compact spheres, the Stokes radius is 30% larger than the radius of gyration (*39*). Further complicating is the fact that neutron scattering would provide an average radius for mixtures of monomers and dimers (*40*). Overall, the numbers of the radius of gyration and the Stokes radii determined in the present study seem consistent, considering slight residual curvature in the Guinier plots, as well as the shape of the pair distribution function in the neutron-scattering study (*17*). However, a detailed comparison appears problematic because of differences of buffer conditions and partial aggregation detected in ref *17*. For IRP2, despite the insertion of the 73 amino acid iron degradation domain in comparison to IRP1, the gross solution structure of IRP2 appears slightly more compact with a Stokes radius of 4.1 nm.

Qualitatively consistent with the results of Brazzolotto et al. (*17*), we have detected an overall conformational change of IRP1 when binding IRE ligand, leading to a compaction of the protein. Similar results were found with IRE binding to IRP2, which showed a decrease in the Stokes radius by 10% upon complex formation. For both IRPs, the change in the overall hydrodynamic shape was accompanied by changes in the protein secondary structure. While the overall structural elements are typical of α/β proteins, a reduced negative ellipticity at 210−220 nm and an increase in the positive ellipticity at 200 nm was observed in the presence of IRE. Similar changes in ellipticity were observed for IRE binding by IRP1 and IRP2, indicating that the structural rearrangement reflected in ellipticity measurements is likely not associated with the shift in IRP1 self-association that accompanies IRE binding. However, differences in the conformation of monomers and dimers that cannot be discerned by CD may exist. The kinetics of the monomer−dimer interconversion of apo-IRP1 was very slow. Slow equilibration of self-associating protein species points toward an energetic barrier between monomer and dimer states and is not uncommon (e.g., see ref *41*).

Open and closed states of the putative ligand-binding cleft were proposed to involve conformational changes around the hinge loop (*2*), with the "open" RNA-binding form differentiated from the "closed" form by the absence of an associated [4Fe−4S] cluster. It is unclear if the presence of a [4Fe−4S] cluster would simply stabilize the protein in the hydrodynamically overall more extended form (with dimerization of IRP1) or induce a third conformation distinct from the two observed in the presence study. The "open" putative binding cleft and higher accessibility to proteolysis (*16*) in the RNA-binding form would not necessarily conflict with a more compact overall hydrodynamic shape.

As far as we know, IRPs are structurally unique in terms of their RNA-binding properties because they do not contain any currently known RNA recognition motifs. We have observed very similar hydrodynamic shapes and secondary structure changes for both IRE and RNA with complementary sequence, suggesting that contributions other than base-specific interactions may contribute at least to initial binding and induction of the conformational change. Shape selectivity has recently been reported for the RNA recognition of cysteinyl-tRNA synthetase (*42*). Interestingly, in the present

case, the binding of oligonucleotide of IRE-C missing the hairpin loop was sufficient to induce a similar, although not completely identical, conformational change in the IRP2 protein. On the other hand, the observation that IRP2 in complex with the complementary IRE-N exhibits a lower lifetime as compared to IRE-C is consistent with previous work (*33*−*35*, *43*, *44*) and suggests that base specificity, which may result from interactions with the hairpin loop bases and/or the bulge C, is important for the complex stability. Overall, it appears that energetic contributions from different features including charge, shape, and base-specific contacts may play a role in different aspects of the protein−RNA complex formation. In the present paper, we have focused on the conformational states of the protein, and although all ligand interactions examined were of high affinity (K_D estimated to be in nanomolar range or tighter), we have not attempted to measure the relative affinities, because the biophysical methods employed here require micromolar concentrations. Further studies and crystallographic data will be needed to fully elucidate the energetic aspects and the mechanism of binding. Nevertheless, it appears that knowledge and consideration of the conformational flexibility of IRP1 and IRP2 will be important for the detailed understanding of the structure and function of the IRPs.

The SV experiments of IRP1 clearly shows the presence of monomers and dimers of IRP1. To our knowledge, this is the first report of self-association of IRPs. In mouse macrophage cells, the total concentration of IRP1 is estimated to be between 0.1 and 1 μM, which is in the range of our estimated dimer dissociation equilibrium constant (Ghosh and Rouault, unpublished data). Although it is difficult to relate *in vitro* data on binding constants to *in vivo* conditions, the abundance of IRP1 supports a functional role of the dimerization. In theory, other ligands stabilizing the different oligomeric states would provide a mechanism to modulate the protein function without altering the expression level. For example, it has been hypothesized that phosphorylation by protein kinase C may exert such a regulatory function on IRP1 (*16*). Interestingly, the cellular abundance of IRP2, which we found to be a stable monomer in contrast to IRP1, is more strongly dependent on cellular iron status than IRP1 (*3*). Because the IRPs function as a central regulator affected by multiple cellular factors, it is likely that they can exist in multiple states. We propose that the monomer−dimer transition may represent an additional regulatory element. Our data show that IRE binding is correlated with changes in the oligomeric state. Further studies are needed to clarify the influence of other ligands with regard to a preferential interaction with the monomeric or dimeric state.

REFERENCES

1. Andrews, N. C. (2000) Iron homeostasis: Insights from genetics and animal models, *Nat. Rev. Genet. 1*, 208−217.
2. Rouault, T., and Klausner, R. (1997) Regulation of iron metabolism in eukaryotes, *Curr. Top. Cell. Regul. 35*, 1−19.
3. Eisenstein, R. S. (2000) Iron regulatory proteins and the molecular control of mammalian iron metabolism, *Annu. Rev. Nutr. 20*, 627−662.
4. Gruer, M. J., Artymiuk, P. J., and Guest, J. R. (1997) The aconitase family: Three structural variations on a common theme, *Trends Biochem. Sci. 22*, 3−6.
5. Klausner, R. D., Rouault, T. A., and Harford, J. B. (1993) Regulating the fate of mRNA: The control of cellular iron metabolism, *Cell 72*, 19−28.
6. Iwai, K., Drake, S. K., Wehr, N. B., Weissman, A. M., LaVaute, T., Minato, N., Klausner, R. D., Levine, R. L., and Rouault, T. A. (1998) Iron-dependent oxidation, ubiquitination, and degradation of iron regulatory protein 2: Implications for degradation of oxidized proteins, *Proc. Natl. Acad. Sci. U.S.A. 95*, 4924−4928.
7. Iwai, K., Klausner, R. D., and Rouault, T. A. (1995) Requirements for iron-regulated degradation of the RNA binding protein, iron regulatory protein 2, *EMBO J. 14*, 5350−5357.
8. Yamanaka, K., Ishikawa, H., Megumi, Y., Tokunaga, F., Kanie, M., Rouault, T. A., Morishima, I., Minato, N., Ishimori, K., and Iwai, K. (2003) Identification of the ubiquitin-protein ligase that recognizes oxidized IRP2, *Nat. Cell Biol. 5*, 336−340.
9. Bourdon, E., Kang, D. K., Ghosh, M. C., Drake, S. K., Wey, J., Levine, R. L., and Rouault, T. A. (2003) The role of endogenous heme synthesis and degradation domain cysteines in cellular iron-dependent degradation of IRP2, *Blood Cells, Mol. Dis. 31*, 247−255.
10. Hanson, E. S., Rawlins, M. L., and Leibold, E. A. (2003) Oxygen and iron regulation of iron regulatory protein 2, *J. Biol. Chem. 278*, 40337−40342.
11. Wang, J., Chen, G., Muckenthaler, M., Galy, B., Hentze, M. W., and Pantopoulos, K. (2004) Iron-mediated degradation of IRP2, an unexpected pathway involving a 2-oxoglutarate-dependent oxygenase activity, *Mol. Cell. Biol. 24*, 954−965.
12. Hanson, E. S., Foot, L. M., and Leibold, E. A. (1999) Hypoxia post-translationally activates iron-regulatory protein 2, *J. Biol. Chem. 274*, 5047−5052.
13. Hanson, E. S., and Leibold, E. A. (1999) Regulation of the iron regulatory proteins by reactive nitrogen and oxygen species, *Gene Expr. 7*, 367−376.
14. Gegout, V., Schlegl, J., Schlager, B., Hentze, M. W., Reinbolt, J., Ehresmann, B., Ehresmann, C., and Romby, P. (1999) Ligand-induced structural alterations in human iron regulatory protein-1 revealed by protein footprinting, *J. Biol. Chem. 274*, 15052−15058.
15. Phillips, J. D., Guo, B., Yu, Y., Brown, F. M., and Leibold, E. A. (1996) Expression and biochemical characterization of iron regulatory proteins 1 and 2 in *Saccharomyces cerevisiae*, *Biochemistry 35*, 15704−15714.
16. Schalinske, K. L., Anderson, S. A., Tuazon, P. T., Chen, O. S., Kennedy, M. C., and Eisenstein, R. S. (1997) The iron−sulfur cluster of iron regulatory protein 1 modulates the accessibility of RNA binding and phosphorylation sites, *Biochemistry 36*, 3950−3958.
17. Brazzolotto, X., Timmins, P., Dupont, Y., and Moulis, J. M. (2002) Structural changes associated with switching activities of human iron regulatory protein 1, *J. Biol. Chem. 277*, 11995−12000.
18. Allerson, C. R., Martinez, A., Yikilmaz, E., and Rouault, T. A. (2003) A high-capacity RNA affinity column for the purification of human IRP1 and IRP2 overexpressed in *Pichia pastoris*, *RNA 9*, 364−374.
19. Trinh, L. B., Phue, J. N., and Shiloach, J. (2003) Effect of methanol feeding strategies on production and yield of recombinant mouse endostatin from *Pichia pastoris*, *Biotechnol. Bioeng. 82*, 438−444.
20. Campanella, A., Levi, S., Cairo, G., Biasiotto, G., and Arosio, P. (2004) Blotting analysis of native IRP1: A novel approach to distinguish the different forms of IRP1 in cells and tissues, *Biochemistry 43*, 195−204.
21. Schuck, P. (2000) Size distribution analysis of macromolecules by sedimentation velocity ultracentrifugation and Lamm equation modeling, *Biophys. J. 78*, 1606−1619.
22. Lamm, O. (1929) Die Differentialgleichung der Ultrazentrifugierung, *Ark. Mat. Astron. Fys. 21B(2)*, 1−4.
23. Schuck, P. (1998) Sedimentation analysis of noninteracting and self-associating solutes using numerical solutions to the Lamm equation, *Biophys. J. 75*, 1503−1512.
24. Dam, J., and Schuck, P. (2004) Calculating sedimentation coefficient distributions by direct modeling of sedimentation velocity profiles, *Methods Enzymol. 384*, 185−212.
25. Schuck, P., and Demeler, B. (1999) Direct sedimentation analysis of interference optical data in analytical ultracentrifugation, *Biophys. J. 76*, 2288−2296.
26. Dam, J., Velikovsky, C. A., Mariuzza, R., Urbanke, C., and Schuck, P. (2005) Sedimentation velocity analysis of protein−protein interactions: Lamm equation modeling and sedimentation coefficient distributions *c*(*s*), *Biophys. J.*, in press.
27. www.analyticalultracentrifugation.com/sedphat/sedphat.htm.

28. Vistica, J., Dam, J., Balbo, A., Yikilmaz, E., Mariuzza, R. A., Rouault, T. A., and Schuck, P. (2004) Sedimentation equilibrium analysis of protein interactions with global implicit mass conservation constraints and systematic noise decomposition, *Anal. Biochem. 326*, 234−256.
29. Sreerama, N., and Woody, R. W. (1993) A self-consistent method for the analysis of protein secondary structure from circular dichroism, *Anal. Biochem. 209*, 32−44.
30. Provencher, S. W., and Glockner, J. (1981) Estimation of globular protein secondary structure from circular dichroism, *Biochemistry 20*, 33−37.
31. Johnson, W. C. (1999) Analyzing protein circular dichroism spectra for accurate secondary structures, *Proteins 35*, 307−312.
32. Gdaniec, Z., Sierzputowska-Gracz, H., and Theil, E. C. (1999) Iron regulatory element and internal loop/bulge structure for ferritin mRNA studied by cobalt(III) hexammine binding, molecular modeling, and NMR spectroscopy, *Biochemistry 38*, 5676.
33. Addess, K. J., Basilion, J. P., Klausner, R. D., Rouault, T. A., and Pardi, A. (1997) Structure and dynamics of the iron responsive element RNA: Implications for binding of the RNA by iron regulatory binding proteins, *J. Mol. Biol. 274*, 72−83.
34. Barton, H. A., Eisenstein, R. S., Bomford, A., and Munro, H. N. (1990) Determinants of the interaction between the iron-responsive element-binding protein and its binding site in rat L-ferritin mRNA, *J. Biol. Chem. 265*, 7000−7008.
35. Allerson, C. R., Cazzola, M., and Rouault, T. A. (1999) Clinical severity and thermodynamic effects of iron-responsive element mutations in hereditary hyperferritinemia-cataract syndrome, *J. Biol. Chem. 274*, 26439−26447.
36. Johnson, W. C. (1996) in *Circular Dichroism and the Conformational Analysis of Biomolecules* (Fasman, G. D., Ed.) pp 433−468, Plenum Press, New York.
37. Tinoco, I., Jr., Mickols, W., Maestre, M. F., and Bustamante, C. (1987) Absorption, scattering, and imaging of biomolecular structures with polarized light, *Annu. Rev. Biophys. Biophys. Chem. 16*, 319−349.
38. Gray, D. M. (2000) in *Circular Dichroism* (Berova, N., Nakanishi, K., and Woody, R. W., Eds.) pp 769−796, Wiley and Sons, New York.
39. Gualfetti, P. J., Iwakura, M., Lee, J. C., Kihara, H., Bilsel, O., Zitzewitz, J. A., and Matthews, C. R. (1999) Apparent radii of the native, stable intermediates and unfolded conformers of the α-subunit of tryptophan synthase from *E. coli*, a TIM barrel protein, *Biochemistry 38*, 13367−13378.
40. Svergun, D. I., and Koch, M. H. J. (2003) Small-angle scattering studies of biological macromolecules in solution, *Rep. Prog. Phys. 66*, 1735−1782.
41. Snyder, D., Lary, J., Chen, Y., Gollnick, P., and Cole, J. L. (2004) Interaction of the trp RNA-binding attenuation protein (TRAP) with anti-TRAP, *J. Mol. Biol. 338*, 669−682.
42. Hauenstein, S., Zhang, C. M., Hou, Y. M., and Perona, J. J. (2004) Shape-selective RNA recognition by cysteinyl-tRNA synthetase, *Nat. Struct. Mol. Biol. 11*, 1134−1141.
43. Theil, E. C., and Eisenstein, R. S. (2000) Combinatorial mRNA regulation: Iron regulatory proteins and iso-iron-responsive elements (Iso-IREs), *J. Biol. Chem. 275*, 40659−40662.
44. Meehan, H. A., and Connell, G. J. (2001) The hairpin loop but not the bulged C of the iron responsive element is essential for high affinity binding to iron regulatory protein-1, *J. Biol. Chem. 276*, 14791−14796.

BI0500325